Hollow SiC@MnO_2 nanospheres with tunable core size and shell thickness for excellent electromagnetic wave absorption

Jinyan Wang[a,b,c], Jintang Zhou[b,*], Harm Van Zalinge[a], Zhengjun Yao[b,*], Li Yang[c,**]

[a] Department of Electrical Engineering and Electronics, University of Liverpool, Liverpool, L69 3GJ, United Kingdom

[b] College of Materials Science and Technology, Nanjing University of Aeronautics and Astronautics, Nanjing, 211100, Jiangsu, People's Republic of China

[c] Department of Chemistry, Xi'an Jiaotong-Liverpool University, Suzhou, 215123, Jiangsu, People's Republic of China

[*] Corresponding author. College of Materials Science and Technology, Nanjing University of Aeronautics and Astronautics, Nanjing, 211100, Jiangsu, People's Republic of China.

[**] Corresponding author. Department of Chemistry, Xi'an Jiaotong-Liverpool University, Suzhou, 215123, Jiangsu, People's Republic of China

Email: yaozj1921@126.com (Z. Yao), imzjt@126.com (J. Zhou), li.yang@xjtlu.edu.cn (L. Yang)

Abstract

The hollow microstructure can permit more incident waves to enter the absorber and increase the attenuation ability by multiple reflections and diffraction. In addition, different substances can introduce the heterogeneous interface and further attenuate electromagnetic waves through interfacial polarisation relaxation. Here, hollow SiC@MnO_2 nanospheres are synthesised with tunable hollow SiC core size and flower-like layered MnO_2 shell thickness. By adjusting the concentration of $KMnO_4$, different shell thicknesses of hollow SiC@MnO_2 nanospheres can be prepared, ranging from 40 nm to 110 nm. Furthermore, hollow SiC@MnO_2 composites with different inner diameters between 300 nm to 470 nm can be obtained by tailoring the amount of tetraethyl orthosilicate. The results indicate that the effective absorbing bandwidth of hollow SiC@MnO_2 can reach 5.71 GHz with a core size of 360 nm and a shell thickness of 90 nm at only 1.8 mm. This work provides a valuable core-shell strategy of hollow SiC@MnO_2 towards excellent electromagnetic wave-absorbing properties.

Keywords: H-SiC@MnO_2 composite, core-shell, hollow, absorber, electromagnetic wave

1 Introduction

As stepping into a new era of fifth-generation technology, web-connected devices and wireless equipment are everywhere. Along with those advances, a consequence is that a new electromagnetic wave (EMW) pollution is exposing living organisms to potential health risks. To decrease the radiation and minimise harmful effects, researchers have increasingly engaged in finding various EMW absorption materials, including carbon-based materials [1-4], magnetic components [5-7], conductive polymers [8-11], and ferrite [12, 13]. However, challenges remain, and the practical applications are not straightforward. Silicon carbide (SiC) has been widely used in the field of EMW absorption due to its high-temperature oxidation resistance, high melting point, high strength, low thermal expansion, low density, and good chemical inertness [14]. The electromagnetic wave absorption performance of pure SiC is poor [15-17]. Hence, hollow structures [18, 19] and compounding with other materials [20-22] have been studied to improve its electromagnetic absorption performance. More attractively, the hollow structure can further lower the weight of the products, which can achieve low mass density and a thinner absorber.

The wide attention to core-shell structure mainly lies in the diverse composition and heterogeneous microstructure. For instance, Zhong et al. [23] synthesised bulk core-shell SiC@Ti_3SiC_2 through molten salt and the effective absorption bandwidth reached 5.6 GHz at 2.3 mm. Yan et al. [24] employed one-step chemical vapour infiltration to grow SiC nanowires on the surface of carbon fibres and improved the EMW absorbing performance of carbon fibres from -5.58 dB to -45.98 dB. Very recently, some reports have been detailing the use of magnetic materials as the core to further enhance the EMW absorption ability. For example, Li et al. [25] prepared flower-like core-shell Fe/Fe_4N@SiO_2 composites with the widest effective absorption

bandwidth of 6.1 GHz at 1.16 mm. It is widely accepted that there are many choices of materials and preparation methods for different core-shell structures and morphology to improve the EMW properties of the composites. Commonly, the EMW absorption ability with fixed components can be adjusted through the shell thickness and core size. And compared with other irregular morphologies, the hollow spherical core-shell structure is easy to obtain the consistency of property because of the isotropic. However, the uniform monodisperse hollow spherical core-shell structure with a tunable core diameter and shell thickness is rarely studied.

MnO_2 is one of the most abundant materials on earth. It has many outstanding advantages, including significant dielectric losses, low cost, good chemical durability and thermal stability, low toxicity and simple preparation methods [26-28]. These unique properties make it a promising EMW absorber [29-31]. Recent reports have also shown that MnO_2 compounding with other materials can further improve EMW absorbing performance [32]. Li et al. [33] successfully prepared MnO_2-covered cotton cloths, and the effective bandwidth is 5.84 GHz at 2.0 mm. Zhang et al. [34] synthesised CoFe@C@MnO_2 hierarchical nanocubes through a MOF-driven process, and the minimum reflection loss is −64 dB at 1.3 mm. Until now, no report has been synthesising hollow SiC@MnO_2 with tunable core size and shell thickness and studying their EMW absorbing performance.

Here in this work, SiO_2 spheres are used as sacrificial templates to prepare hollow SiC. Then MnO_2 is covered with hollow SiC through a hydrothermal strategy to prepare a uniform core-shell hollow SiC@MnO_2 structure. Adjusting the shell thickness and hollow core diameter can obtain a series of hollow SiC@MnO_2 with customised EMW properties. When the shell thickness is 90 nm and the core diameter is 360 nm, the product has the optimal EMW absorbing performance. The

corresponding frequency region with reflection loss lower than −10 dB can reach 5.71 GHz at only 1.8 mm. Our results highlight that the hollow spherical structure combined with shell evolution is a valuable strategy to boost EMW absorbing capacity.

2 Experimental sections

2.1 Materials

Tetraethyl orthosilicate (TEOS, Macklin, China), ammonium hydroxide solution ($NH_3 \cdot H_2O$, 25-28 wt%, Nanjing Reagent, China), ethanol absolute (EtOH, Shanghai LingFeng Chemical Reagent Co., Ltd, China), resorcinol (Macklin, China), formaldehyde (37-40 wt%, Macklin, China), potassium permanganate ($KMnO_4$, Sinopharm Chemical Reagent Co., Ltd, China), hydrofluoric acid (HF, 40 wt%, Macklin, China). All materials, including distilled water (DI) were used without further purification.

2.2 Preparation of uniform hollow SiC (H-SiC)

H-SiC was synthesised through the sacrificial templating method. Firstly, 18 ml TEOS was added to the solution of 400 ml EtOH, 56 ml DI and 24 ml $NH_3 \cdot H_2O$ and magnetically stirred for 1 hour. Secondly, 3.2 g resorcinol and 4.5 ml formaldehyde were added and stirred for another 24 hours. Then the products were put in a tube furnace to react at 1350 ℃ for 4 hours under argon protection. Finally, H-SiC was obtained after etching in 20 wt% HF for 12 hours and unreacted carbon removal at 650 ℃ for 3 hours under an air atmosphere.

2.3 Preparation of tunable shell thickness of H-SiC@MnO_2

H-SiC@MnO_2 were prepared through the hydrothermal method. First, 40 mg H-SiC was added to 10 mM $KMnO_4$ solution and ultrasonic for 30 minutes. Then the mixture was transferred to a 100 ml Teflon and heated at 140 ℃ for 2 hours. The H-

SiC@MnO_2 can be obtained after centrifugation, washed with DI three times and dried at 80 ℃ for 4 hours. In order to adjust the shell thickness of MnO_2, different concentrations of $KMnO_4$ solution were prepared. The resultant core-shell H-SiC@MnO_2 for 5 mM, 10 mM, 20 mM, 40 mM and 60 mM $KMnO_4$ solution was named H-SiC@MnO_2-5, H-SiC@MnO_2-10, H-SiC@MnO_2-20, H-SiC@MnO_2-40 and H-SiC@MnO_2-60, respectively.

2.4 Preparation of controllable size of H-SiC@MnO_2

The size of the sacrificial template determines the size of the hollow core. Different sizes of templates can form by changing the volume of TEOS from 18 ml to 8 ml and 28 ml. After the same reaction and treatment, the different hollow diameters of H-Si@MnO_2 at the same concentration of 10 mM $KMnO_4$ solution can be obtained and labelled as H-SiC@MnO_2-8, H-SiC@MnO_2-18 and H-SiC@MnO_2-28.

2.5 Characterisation

The products' crystalline phases and phase purity were tested by X-ray diffraction (XRD), operated at 40 kV and 40 mA and the 2-theta from 10 ˚ to 80 ˚. The valence of H-SiC@MnO_2 was analysed by an X-ray photoelectron spectrometer (XPS). The microstructure of the products was observed through a field emission scanning electron microscope (FESEM). The hollow morphology was tested on a transmission electron microscope (TEM). The specific surface area and pore size of H-SiC@MnO_2 were tested by a Nitrogen adsorption-desorption analyser (BET). The electromagnetic wave absorption performance was tested by a vector network analyser between 2 GHz and 18 GHz using a circular ring obtained by mixing with paraffin with a filling weight ratio of 35 %.

3 Results and discussion

Figure 1 (a) depicts the preparation process of H-SiC@MnO_2 core-shell

137 composites. Firstly, SiO_2 sphere templates were prepared through the classic Stober
138 method [35]. Figure 1 (b) shows the templates have good uniformity and
139 monodispersity, and the diameter of SiO_2 spheres is around 370 nm. Then, resorcinol
140 and formaldehyde were added to the solution to form SiO_2@RF. The amount of
141 resorcinol and formaldehyde is crucial to the monodispersity of SiO_2@RF. As seen in
142 Figure 1 (c), the condensation reaction of RF resin is coated on the surface of the
143 template, and the spherical size is increased to around 420 nm. However, if the
144 concentration of resorcinol and formaldehyde is high, the microstructure of SiO_2@RF
145 is sea-island, as shown in Figure.S1. Thirdly, SiC can be obtained in the interface
146 between SiO_2 and carbonised RF resin due to the diffusion effect of SiO_2 at 1350 ℃,
147 which follows the vapour-solid mechanism. Figure 1 (d) shows that the spherical
148 structure was maintained after the carbon thermal reduction, but the size shrunk
149 slightly to about 410 nm. Subsequently, H-SiC can be obtained after etching and
150 oxidation treatment. The monodisperse hollow spherical structure is clearly seen in
151 Figure 1 (e, g). The diameter and shell thickness of H-SiC is approximately 390 nm
152 and 25 nm, respectively. Finally, the H-SiC@MnO_2 can be prepared after a
153 hydrothermal reaction. The growth of MnO_2 nanosheets on the surface of hollow SiC
154 is mainly generated by the decomposition and deposition of $KMnO_4$. The produced
155 nanocrystal MnO_2 precipitated on the surface of hollow SiC and covered the whole
156 sphere, acting as a nucleation site to further promote the decomposition of $KMnO_4$.
157 Finally, the nanosheets can be formed after further depositing along the surface of
158 MnO_2. Figure 1 (f, h) show that the surface character significantly changes due to the
159 MnO_2 nanolayer coating, which maintains the hollow structure. The diameter and
160 shell thickness of H- SiC@MnO_2 increase to around 440 nm and 90 nm, respectively.
161 Furthermore, different shell thickness samples were synthesised by adjusting the

concentrations of $KMnO_4$ solution, ranging from 5 mM to 60 mM, and the morphologies are displayed in Figure 2.

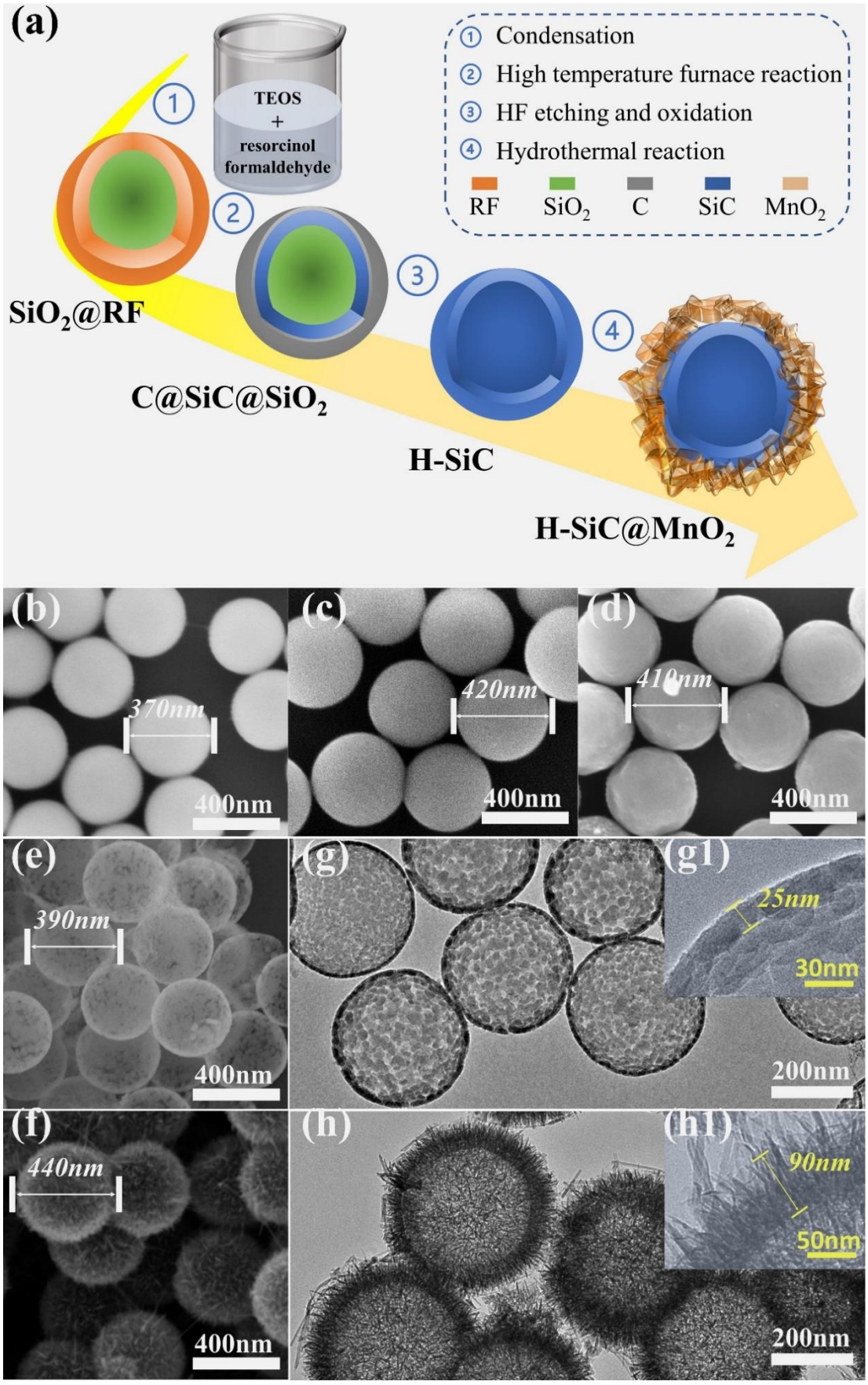

Figure 1 (a) Schematic diagram of the synthesis process of H-SiC@MnO_2 core-shell composites. (b-f) FESEM

images of products in different stages. (b) SiO_2, (c) SiO_2@RF, (d) C@SiC@SiO_2, (e) H-SiC, (f) H-SiC@MnO_2. (g, h) TEM images of H-SiC and H-SiC@ MnO_2.

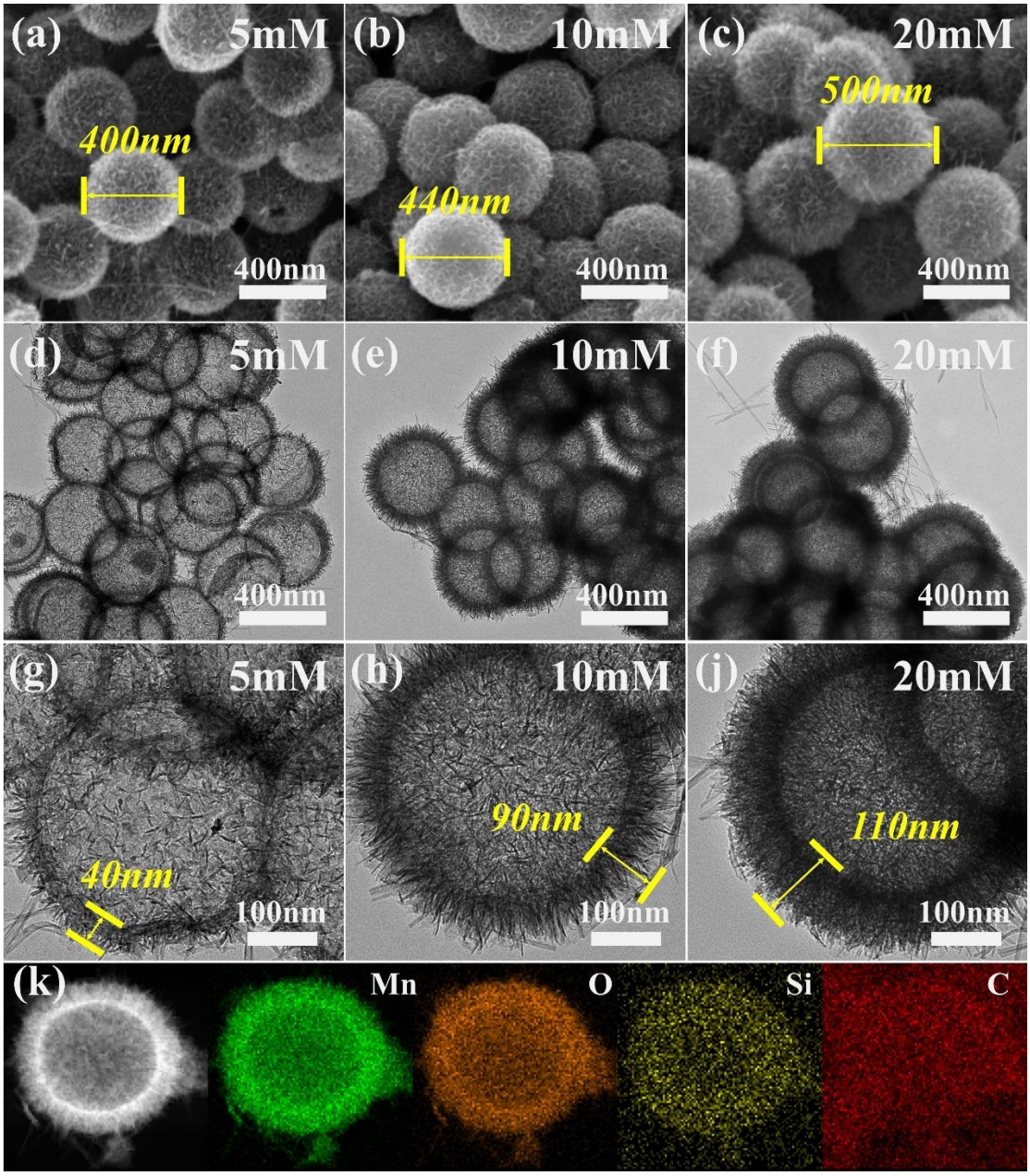

Figure 2 (a-c) FESEM images of different shell thicknesses of H-SiC@MnO_2 composites. (d-j) TEM images of varying shell thickness of H-SiC@MnO_2 composites. (k) elemental mapping distribution of H-SiC@MnO_2-10.

As shown in Figure 2 (a-c), with the concentration of $KMnO_4$ solution increasing from 5 mM to 20 mM, the diameter of the monodisperse spheres presents a slight upward. The particle size of H-SiC@MnO_2-5, 10 and 20 is about 400, 440 and 500 nm, respectively. The FESEM images of H-SiC@MnO_2-40 and H-SiC@MnO_2-60 are shown in Figure.S2. Due to the high concentration of $KMnO_4$, the spheres adhere to

each other, which illustrates poor dispersibility. As shown in Figure 2 (d-j), the core-shell hollow structure can be distinctly seen, and as the concentration of $KMnO_4$ solution climbs, the loading thickness of the MnO_2 layer goes up, which is consistent with the diameter in Figure 2 (a-c). The detailed shell structure is shown in Figure 2 (g-j), and the shell thickness of H-SiC@MnO_2-5, 10 and 20 is approximately 40, 90 and 110 nm, respectively. The elements mapping scan shows that Mn, O, Si and C are uniformly distributed in the shell edge (Figure 2 k). The Si and C are not obvious because they are inside the MnO_2 shell.

As shown in Figure 3 (a), the two diffraction peaks at 37 ˚ and 66 ˚ correspond to the (111) and (020) planes of MnO_2 (JCPDS card no. 44-0141) [36]. SiC did not appear in the XRD spectrum, probably because the MnO_2 coating is relatively thick, and the detection depth of XRD cannot penetrate. For pure H-SiC, the XRD pattern is shown in Figure.S3. XPS (Figure 3 b) determined the elemental composition of the prepared H-SiC@MnO_2 and confirmed the presence of Mn, C, O and Si in the H-SiC@MnO_2 composites. The detail scan spectra observed the more detailed functional groups on each element (Figure 3 c-f). From Figure 3 (c), the C1*s* display three fitting peaks at 283.8, 284.8 and 286.8 eV corresponding to the C-Si, C-C and C-O, respectively [37]. The Mn 2*p* spectrum in Figure 3 (d) shows two prominent peaks at 642.2 and 653.8 eV, coinciding with Mn $2p_{3/2}$ and Mn $2p_{1/2}$, respectively [38]. In addition, the valence state of Mn is +4 due to the spin energy separation of Mn 2*p* being 11.6 eV [33]. The fitting peaks at 530.2, 532.2 and 533.3 eV correspond to Mn-O, C-O and H-O-H groups (Figure 3 e) [39]. At the same time, there is only one central peak in Si 2*p* at 101.1 eV, which belongs to Si-C bonding (Figure 3 f) [20].

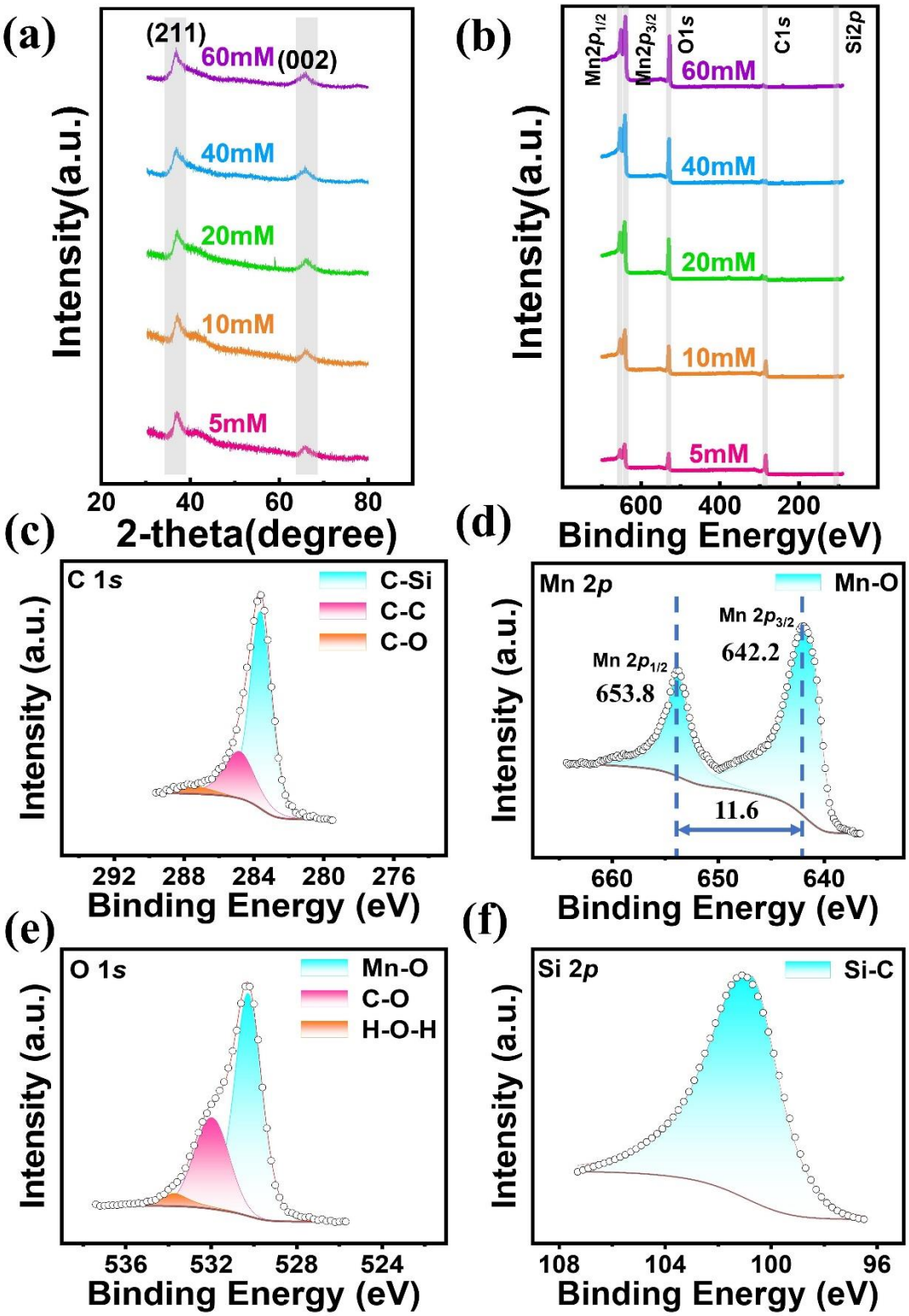

Figure 3 (a) The XRD patterns of H-SiC@MnO_2 composites. (b) XPS survey scan of H-SiC@MnO_2 composites. (c-f) XPS detail scan of H-SiC@MnO_2-10 composite. (c) C 1*s*, (d) Mn 2*p*, (e) O 1*s*, (f) Si 2*p*.

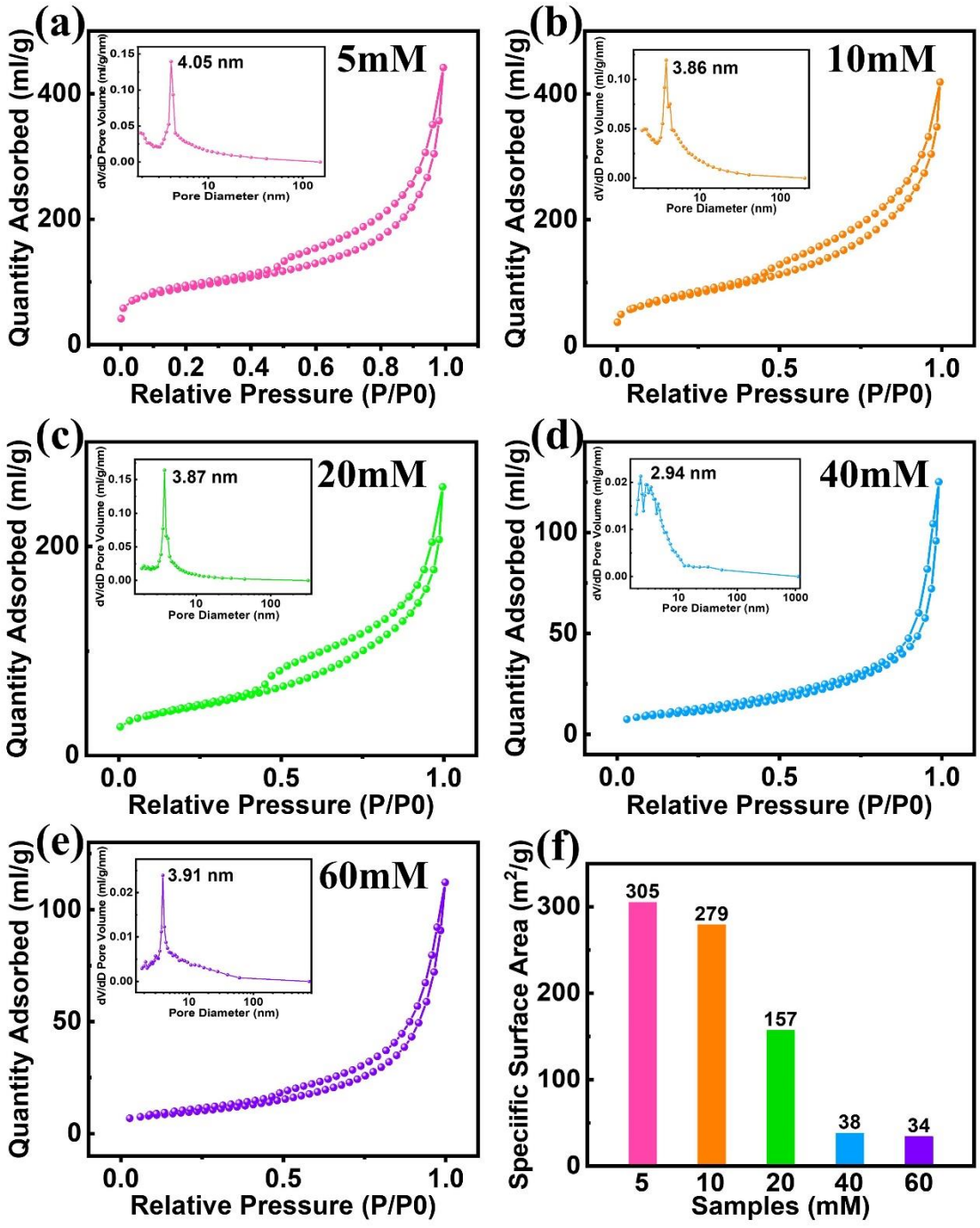

Figure 4 Nitrogen adsorption-desorption curves of H-SiC@MnO_2 composites. (a) H-SiC@MnO_2-5, (b) H-SiC@MnO_2-10, (c) H-SiC@MnO_2-20, (d) H-SiC@MnO_2-40, (e) H-SiC@MnO_2-60. Insets in (a-e) are the corresponding pore diameter distribution curves. (f) The specific surface area of each composite is in the bar chart.

The specific surface area and porosity of H-SiC@MnO_2 composites were analysed using Nitrogen adsorption-desorption BET (Figure 4). As seen in Figure 4 (a-e), when the relative pressure P/P_0 is greater than 0.5, the absorbed quantity soars, showing a typical Ⅳ type adsorption isotherm curve and H3 type hysteresis ring, which indicates

capillary condensation and containing mesoporous in the composite [40]. The BET method calculated the specific surface area of each composite and is shown in Figure 4 (f). With the increasing MnO_2 shell thickness, the specific surface area value decreased, changing from 305 $m^2 \cdot g^{-1}$ for H-SiC@MnO_2-5 to 34 $m^2 \cdot g^{-1}$ for H-SiC@MnO_2-60. The drop in specific surface area value was primarily due to the adhesion of spheres and the high density of MnO_2. In theory, the larger the specific surface area of the material, the greater the number of atoms on the surface, which are more likely to polarise and lead to polarisation loss [41]. The specific absorption performance of the composite is discussed as follows.

The influence of different shell thicknesses of H-SiC@MnO_2 composites on the EMW properties is determined based on the transmission-line theory. For single layer absorber, the reflection loss (RL) can be calculated as follows [42, 43]:

$$RL = 20\, log_{10}|(Z_{in} - Z_0) \,/\, (Z_{in} + Z_0)| \quad (1)$$

$$Z_{in} = Z_0\sqrt{\mu_r/\varepsilon_r}\, tanh[j(2\pi f d/c)\sqrt{\mu_r\varepsilon_r}] \quad (2)$$

where $Z_0 = (\mu_0 \,/\, \varepsilon_0)^{1/2} = 120\pi = 377\Omega$, Z_0 means the free space impedance. Z_{in} represents the input impedance of the absorber. ε_r ($\varepsilon_r = \varepsilon' - i\varepsilon''$) and μ_r ($\mu_r = \mu' - i\mu''$) are complex permittivity and complex permeability, respectively. f is the frequency. d is the thickness of the absorber, and c is the propagation velocity of EMW in free space. The frequency bandwidth in which the RL is less than -10 dB is expressed by ΔW_{10}, corresponding to 90 % of the EMW energy absorbed. Thus, ΔW_{10} is used to measure the effective absorption bandwidth. Based on Equations (1) and (2), the RL of different concentrations of H-SiC@MnO_2 composites were calculated, and the results can be seen in Figure 5. For 0 mM (pure H-SiC) and 5 mM H-SiC@MnO_2 composites, the highest filling ratio of the tested ring is only 20 wt% due to the soft trait. For other H-SiC@MnO_2 composites (10 mM, 20 mM, 40 mM and 60

mM), the filling ratio is 35 wt%. The 3D colourmap surface plot with the projection of the reflection loss of each sample is shown in Figure.S4. As seen in Figure 5 (a-f), adding the MnO_2 shell can improve the absorbing strength and widen the absorption bandwidth of the composites. The minimum RL (RL_{min}) of H-SiC@MnO_2-0, 5, 10, 20, 40 and 60 is -29, -45, -47, -61, -46, and -51 dB, respectively. The region within the dotted line represents the effective absorption bandwidth of each composite in the range of 1-10 mm. Among them, H-SiC@MnO_2-10 and H-SiC@MnO_2-20 can achieve EMW absorbing properties in the entire frequency range, and the smaller the frequency, the greater the thickness. The reason is that the wavelength increases as the frequency decreases, leading to the longer distance the EMW travels in the same period, which needs a higher thickness [44]. Figure 5 (g-k) clearly shows the better EMW performance of H-SiC@MnO_2-10 and H-SiC@MnO_2-20 composites. The ΔW_{10} of H-SiC@MnO_2-10 and H-SiC@MnO_2-20 were measured to be 5.71 GHz and 4.57 GHz at only 1.8 mm and 1.6 mm, respectively, which improved by 225 % and 180 % compared to the pure H-SiC (ΔW_{10}=2.54 GHz at 10 mm).

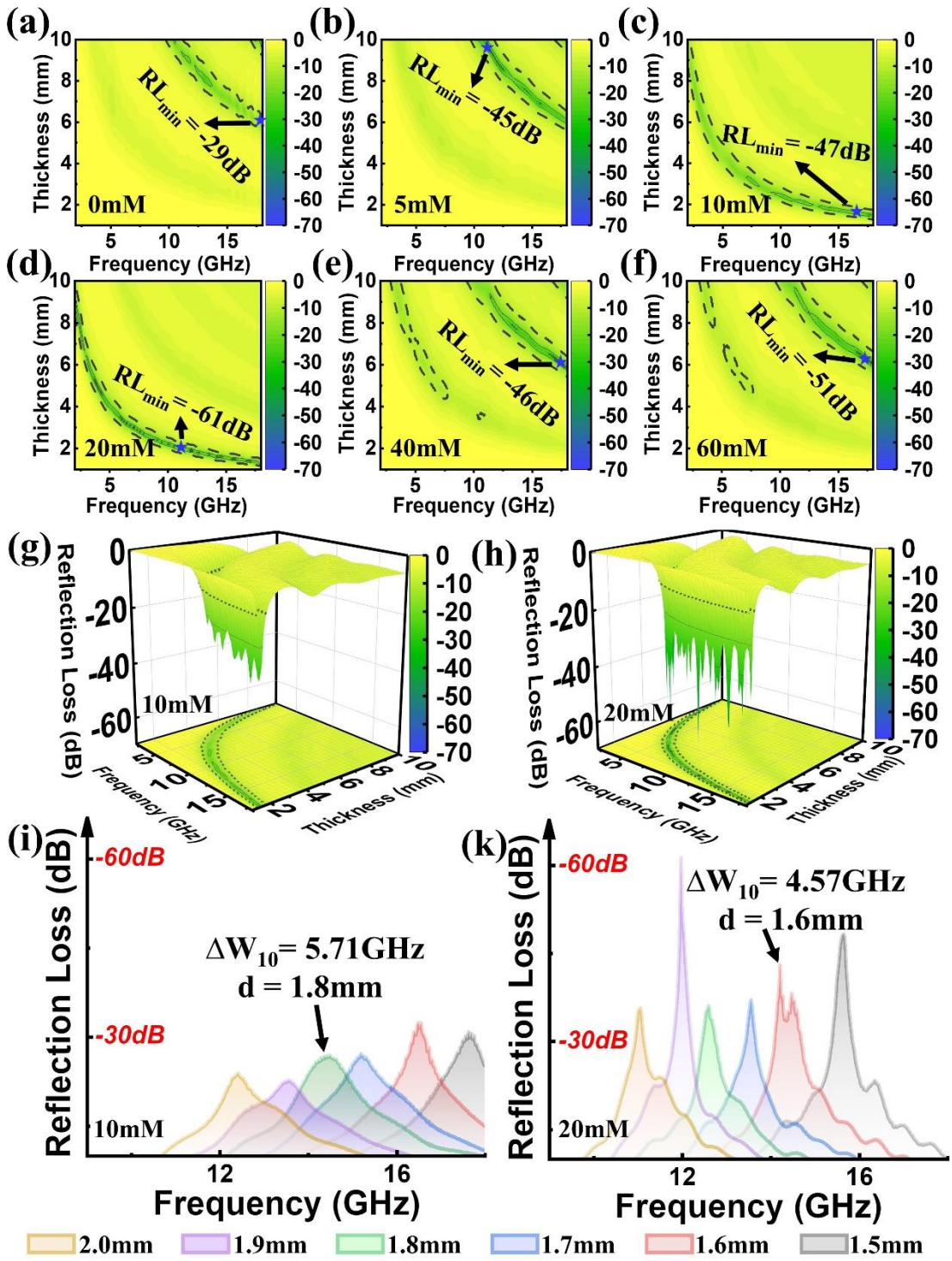

Figure 5 (a-f) The 2D colour-filled contour plots of reflection loss of pure H-SiC (0mM) and different concentrations of H-SiC@MnO_2 composites. (g-h) The 3D colourmap surface plot with the projection of reflection loss of H-SiC@MnO_2-10 and H-SiC@MnO_2-20 composites. (i-k) The reflection loss curves of H-SiC@MnO_2-10 and H-SiC@MnO_2-20 composites at different thicknesses.

As thin interference-absorbing material, the absorption intensity and bandwidth are controlled by electromagnetic parameters. SiC and MnO_2 are non-magnetic

materials; therefore, complex permeability and magnetic loss are not affected. The complex permittivity was studied to explain the improved EMW performance of H-SiC@MnO_2 composites and the curves are shown in Figure 6. With the increase of the concentration of $KMnO_4$, the dielectric constant of H-SiC@MnO_2 composites increased at first and then decreased, which is due to the changes in the scattering effect of the hollow spheres in paraffin. If the concentration of $KMnO_4$ was above 40 mM, agglomeration would happen, leading to decreased scattering effect and lower dielectric constant. When the concentration falls below 40 mM, the hollow spherical composites have a good dispersity, and the scattering effect increases with the larger spheres, resulting in a higher dielectric constant. The complex permittivity (ε' and ε'') of each sample tends to increase with the decrease in frequency, which can result in a widened frequency bandwidth. Furthermore, the faster the increase, the more pronounced the broad bandwidth is [45, 46]. The results in Figure 6 (a) present the ε' value increase from 5.5 at 0 mM to 17.1 at 20 mM; however, it then decreases to 6.2 at 60 mM with the rising thickness of the MnO_2 shell. H-SiC@MnO_2-20 shows the fastest variation trend from 10.5 to 17.1, while H-SiC (0 mM) present the lowest increase trend from 4.3 to 5.5. In addition, the ε' value and growth trend of H-SiC@MnO_2-10 are very close to the H-SiC@MnO_2-20 product, which rises from 8.3 to 15.2. The ε'' value and dielectric loss tangent ($\tan\delta_\varepsilon$) present the similar tendency except for the composite at the concentration of 10 mM, which has the highest ε'' value of 7.2 and the biggest $\tan\delta_\varepsilon$ value at 0.54. Meanwhile, as observed in Figure 6 (b), there are three peaks exist in ε'' curves, which represent multiple relaxation processes due to the interface polarisation and dipole polarisation [47, 48]. The numbers and positions are consistent well with the Cole-Cole curves in Figure.S5, and each semicircle presents the Debye relaxation process. There are two semicircles for

pure hollow SiC (0 mM), which may be due to dipole polarisation coming from defects. While for H-SiC@MnO_2 composites, three semicircles can be observed, demonstrating the enhancements of the Debye relaxation process, which are put down to the interfacial polarisation between SiC and MnO_2 [49, 50]. Furthermore, a higher ε'' and $\tan\delta_\varepsilon$ value equates to a more significant dielectric loss capability. Thus, H-SiC@MnO_2-10 possesses the broadest absorbing bandwidth among the composites, which aligns well with the result in Figure 5.

The absorption intensity of single-layer dielectric material is achieved by improving the impedance matching degree, and the complete matching means the total reflection is 0 ($Z_{in} = Z_0$). For pure dielectric material (μ'=1, μ''=0), the relationship between ε', ε'' and d/λ_0 can be expressed as follows [44]:

$$tan\,h\left[j(2\pi d\,/\,\lambda_0)\sqrt{\varepsilon'-\varepsilon''}\right] = \sqrt{\varepsilon'-\varepsilon''} \quad (3)$$

where λ_0 ($\lambda_0 = c\,/\,f$) is the wavelength of EMW in free space. Through Equation (3), the matching value of ε', ε'' and d/λ_0 can be calculated. In theory, if the ε'- ε'' (Cole-Cole) curves of an absorber intersect with the calculated matching curve, the electromagnetic parameters at the intersection are entirely matched, and the EMW absorbing strength is the most significant [51]. If it is outside the matching curve, the electromagnetic parameters do not match, and a minor interference-absorbing peak can be generated. To put it simply, the closer the Cole-Cole plot is to the matching curve, the better the matching condition is and, thus, the stronger the absorption peak. The matching line and Cole-Cole curves of each composite are shown in Figure 6 (d). Curves of H-SiC@MnO_2-10 and H-SiC@MnO_2-20 are close to the matching line, especially the curve of H-SiC@MnO_2-20; as can be seen, it generated a significant number of intersection points with the matching curve, which represents a lot of stronger EMW absorbing peaks. The curve of pure H-SiC (0 mM) is farthest from the

matching curve, and the EMW absorbing strength is weak, which is caused by the lower ε'' value. Furthermore, when the real part of permittivity is low, the range of the matching imaginary part is narrow. When the real part of permittivity is high, the scope of the matching imaginary part is broad [44]. Therefore, the larger the complex permittivity value, the easier it is to achieve matching conditions, resulting in better EMW absorption. The improved EMW absorbing intensity of each composite can be clearly seen in the 3D colour-mapping graphs (Figure.S4), which can be attributed to the enhanced matching condition of ε' and ε'' value due to the introduction of the MnO_2 shell. The particular hollow core-shell structure with different electronegativity can induce interfacial polarisation and boost ε' and ε'' value, which favours the impedance matching and broad absorption bandwidth of the composite absorber. In addition, the hollow cavity not only facilitates the multireflection and multi-scattering in the core but also brings down the density, which endows the composite with an immense amount of filling at the same weight ratio.

According to Debye's theory, Equation (4) is used to quantitatively analyse the proportion of polarisation and conductive loss.

$$\varepsilon'' = \varepsilon_p'' + \varepsilon_c'' = (\varepsilon_s - \varepsilon_\infty)[(\omega\tau)/(1+\omega^2\tau^2)] + \sigma/\omega\varepsilon_0 \quad (4)$$

where ε_s is the static dielectric constant, ε_∞ is the optical dielectric constant, τ is the relaxation time, $\varepsilon_0 = 10^7/4\pi c^2 \approx 8.854 \times 10^{-12} F/m$, ε_0 means the static dielectric constant of free space, σ is conductivity, ε_p'' and ε_c'' represent polarisation loss and conductive loss, respectively. An equivalent circuit can describe the interaction between EMW and absorber, and the ε_c'' can be equivalent to a parallel circuit with a shunt effect, the ε_p'' can be equivalent to a series circuit with a divider effect. The fitted results are displayed in Figure 6 (e-f). The ε_c'' increases with the increase contents of MnO_2, which is mainly due to the micro-current generated by nanoflake

MnO_2 (Figure 6 e). For ε_p'' curves, when the concentration is lower than 40 mM, the ε_p'' value raises with the increase of MnO_2 content which is due to the increase in interface polarisation between MnO_2 and SiC. When the content of MnO_2 further increases, the shell is thicker, and the spheres adhere to each other; thus, the value decreases obviously. Furthermore, when the concentration is lower than 40 mM, the dielectric loss of the H-SiC@MnO_2 composites is dominated by polarisation loss. In contrast, the conductive loss is higher than the polarisation loss when the concentration further increases.

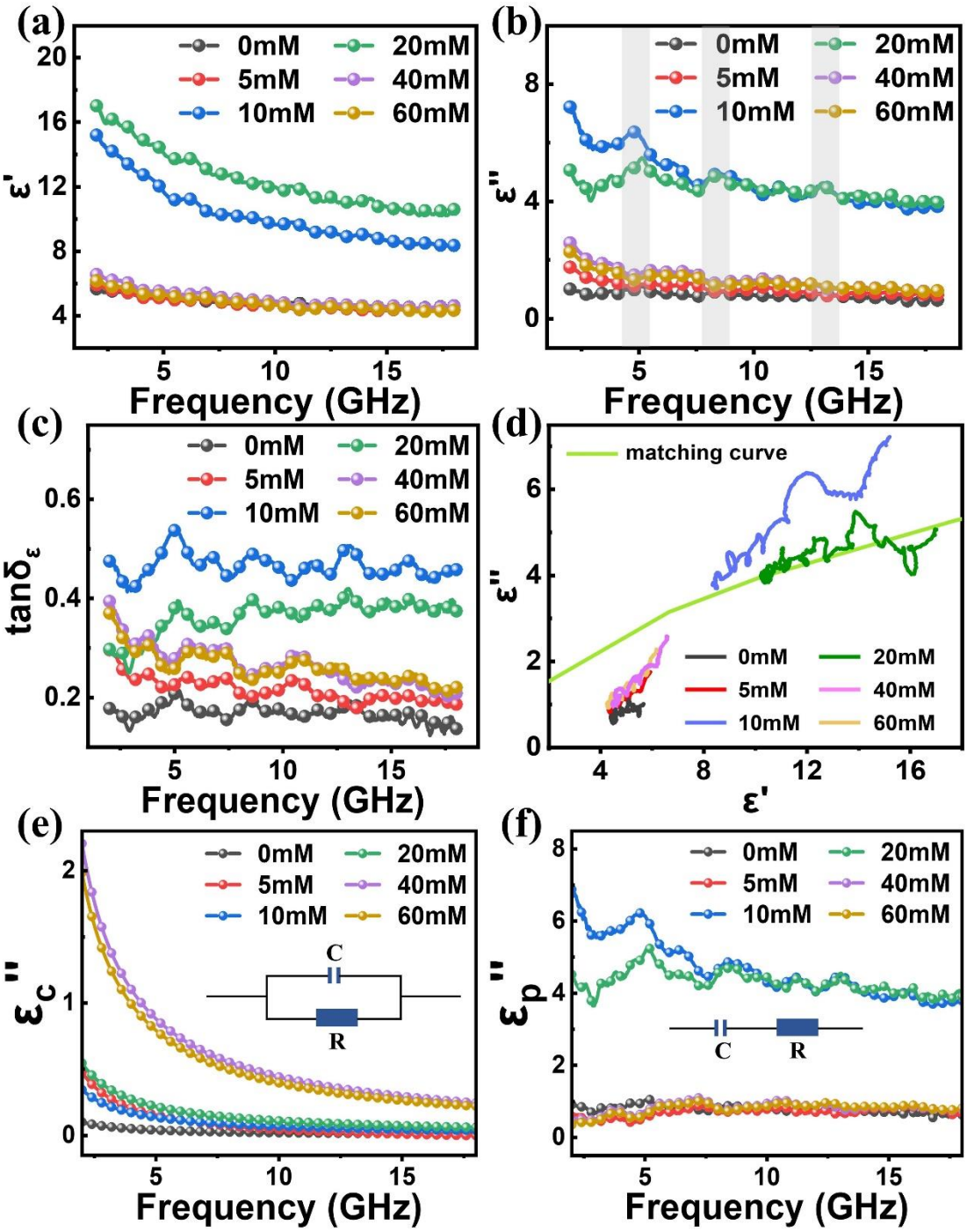

Figure 6 Complex permittivity of different concentrations of H-SiC@MnO_2 composites. (a) real permittivity, (b) imaginary permittivity, (c) dielectric loss tangent, (d) Cole-Cole curves, (g) contribution of conductive loss, (h) contribution of polarisation loss.

To further study the contribution of hollow core size on EMW absorption capabilities, a string of H-SiC@MnO_2 composites with a concentration of 10 mM $KMnO_4$ were prepared with three different volumes (8 ml, 18 ml, and 28 ml) of

TEOS. Figure 7 (a-c) shows that the diameter of SiO_2 templates is 310, 360, and 480 nm when the volume of TEOS changes from 8 ml to 18 ml and further to 28 ml. The silicon sources increase with the high volume of TEOS. Sufficient raw material continuously supplies the condensation nuclei and grows up to larger SiO_2 templates. Then, after a series of reactions and treatment, H-SiC@MnO_2 composites with 390, 440 and 560 nm were synthesised under the different sizes of templates (Figure 7 d-f). The diameters of the templates and final composites are aligned well with the statistical size distribution as shown in Figure.S6, where the average diameter of SiO_2 templates is 309.1, 359.7 and 481.4 nm, the average particle size of H-SiC@MnO_2 composites are 390.1, 440.9 and 561.2 nm, respectively. As seen in Figure 7 (g-l), all the products show a hollow structure and the same shell thickness of 90 nm.

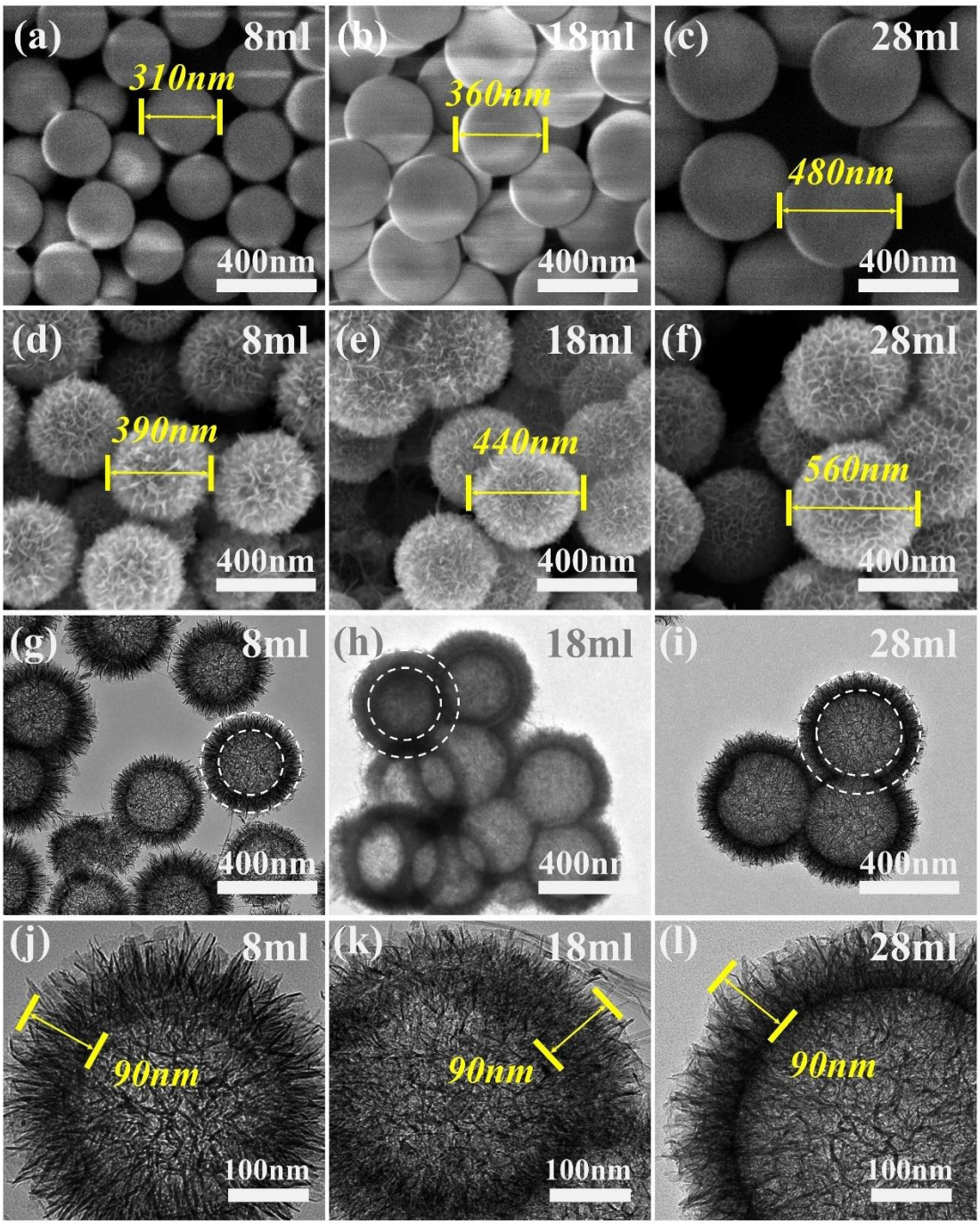

Figure 7 (a-c) FESEM images of different sizes of SiO_2 templates. (d-f) FESEM images of varying core sizes of H-SiC@MnO_2 composites. (g-l) TEM images of different core sizes of H-SiC@MnO_2 composites.

The complex permittivity closely relates to the size of the nanoparticles due to the mutual effect of free electrons. Since the theoretical formula for the size effect on the dielectric medium has not been established, the Euler equation, which describes the size effect on metal particles, is used to analyse the relationship between the complex permittivity and particle size. When the effective average free path of

electrons in the particles equals the particle size, the size effect on the complex permittivity can be calculated as follow [35]:

$$\varepsilon(\omega, r) = \varepsilon'(\omega) + i[\varepsilon''(\omega)] + \left(\omega_p^2 v_f\right) / (\omega^3 r) \quad (5)$$

where ω_p is the plasma frequency of the bulk medium, ω is the electromagnetic wave frequency, v_f is Femi velocity, and r is the radius of the particle. Equation (5) shows that the imaginary permittivity is inversely proportional to the radius of the particles. Therefore, the imaginary permittivity increases with the decrease in particle size. As observed in Figure 8 (a-c), the particle size has a noticeable effect on the dielectric property of H-SiC@MnO_2 composites. The ε' increase from 7.3 at 28 ml to 15.2 at 18 ml, then further rises to 25.7 at 8 ml as the core size decrease. The ε'' value increases from 2.8 at 28 ml to 10.8 at 8 ml as the diameter falls, indicating an increase in the loss capacity. The growth of complex permittivity is because the smaller the particle size, the higher the ratio of atoms on the surface, which are more likely to polarise and thus lead to the increase of permittivity. Even though the smallest H-SiC@MnO_2 composite at 8 ml possesses the highest complex permittivity, its EMW ability is not the best (Figure 8 e-h) due to the poor impedance matching condition. As observed in Figure 8 (d), the Cole-Cole curve of the H-SiC@MnO_2 composite at 18 ml is the closest to the matching curve, which means the best matching condition between ε' and ε''. It is commonly accepted that a well-matched impedance matching condition is a primary condition for designing high-performance EMW absorbers [43, 52]. Especially at a thickness of 1.3-1.8 mm, the ΔW_{10} and RL_{min} of H-SiC@MnO_2 composite at 18 ml can reach 5.7 GHz and -32 dB. In comparison, the two value of H-SiC@MnO_2 composite at 8 ml is only 3.2 GHz and -22 dB, respectively. The results indicate that the H-SiC@MnO_2 composite at 18 ml has the best EMW absorbing performance due to the suitable size.

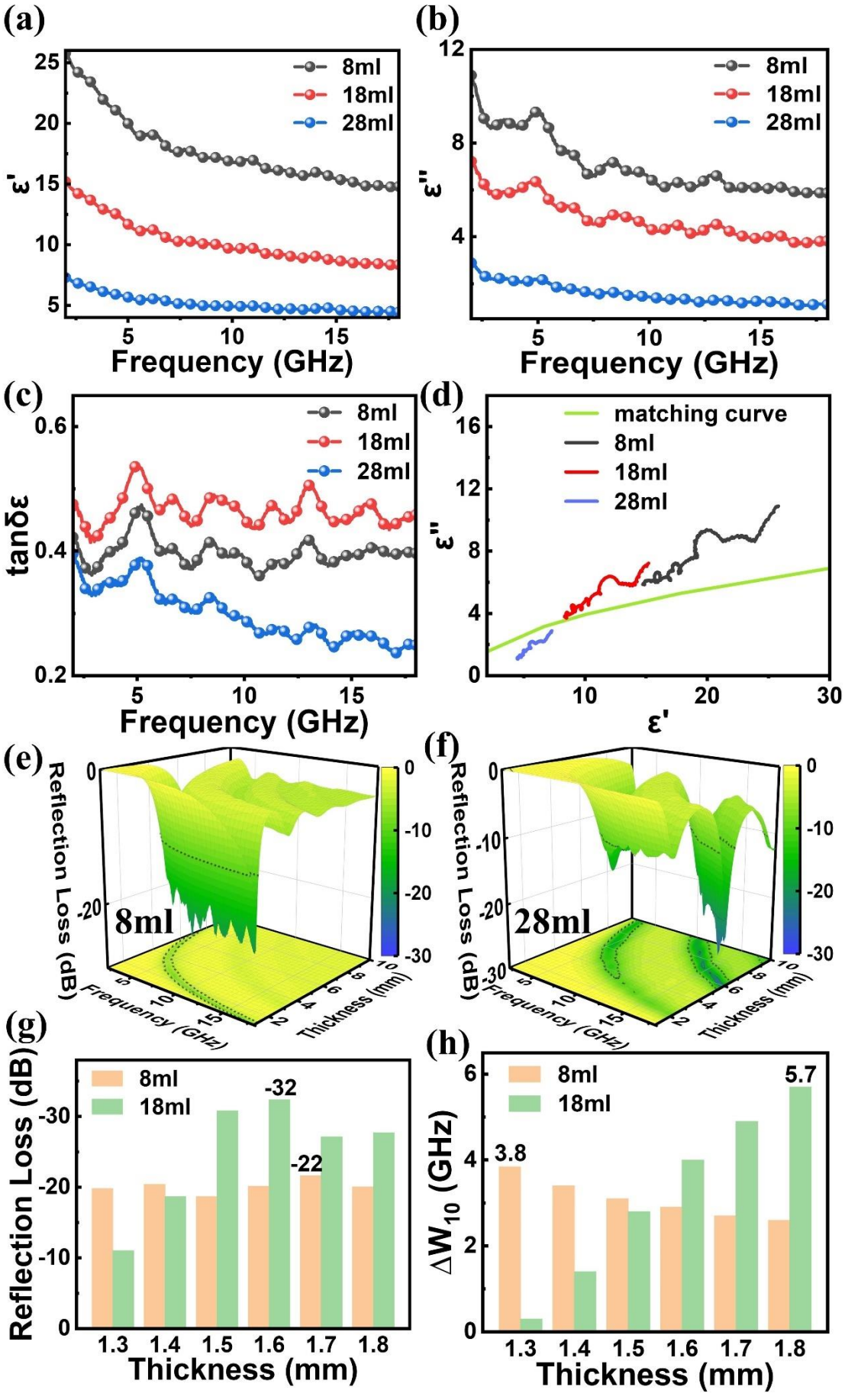
(a)
ε'
Frequency (GHz)
8ml
18ml
28ml
(b)
ε''
Frequency (GHz)
8ml
18ml
28ml
(c)
tanδε
Frequency (GHz)
8ml
18ml
28ml
(d)
ε''
ε'
matching curve
8ml
18ml
28ml
(e)
8ml
Reflection Loss (dB)
Frequency (GHz)
Thickness (mm)
(f)
28ml
Reflection Loss (dB)
Frequency (GHz)
Thickness (mm)
(g)
Reflection Loss (dB)
8ml
18ml
-32
-22
Thickness (mm)
(h)
ΔW10 (GHz)
8ml
18ml
3.8
5.7
Thickness (mm)

391

Figure 8 (a-d) Complex permittivity of the different core sizes of H-SiC@MnO_2 composites. (a) real permittivity, (b) imaginary permittivity, (c) dielectric loss tangent, (d) Cole-Cole curves. (e-f) The 3D colourmap surface plot with the projection of reflection loss of H-SiC@MnO_2-10 at 8 ml and 28 ml. (g-h) The reflection loss and effective absorption bandwidth (ΔW_{10}) of H-SiC@MnO_2-10 composites at different thicknesses at 8 ml and 18 ml.

The EMW absorbing mechanism of the H-SiC@MnO_2 composite is illustrated in Figure 9. Firstly, when the EMW contacts the monodisperse core-shell spheres, the particle can become a source to emit waves. Thus, the incident wave can be divided into three parts: absorbed, propagating, and scattered. Notably, multiple reflections occur when the EMW enters the sphere due to the hollow structure. The multiple scattering, reflection and absorption of the composites significantly attenuate the EMW energy to realise the high-performance absorber. Furthermore, the scattering strength of the particle is closely related to the particle size. If the particle size is appropriately large, the scattering is enhanced, and the attenuation of EMW energy is improved. However, the complex permittivity falls with the growth of particle size. Thus, the particle size to EMW absorbing ability is complex and contradictory. In this work, the medium particle size absorbs the widest EMW. Also, the hollow structure and nanoflower morphology improve the impedance matching condition, which enables more EMW to enter the absorber to be consumed. Secondly, the MnO_2 shell is uniformly coated on the spherical H-SiC, resulting in heterogeneous mass interfaces where free electrons accumulate and generate strong interfacial polarisation to induce dielectric loss. Meanwhile, according to equivalent circuit theory, there are three kinds of conduction loss: (1) the nanosheet MnO_2 shell can form a sizeable conductive network, promoting conductive loss. (2) the electron migration and hopping between the MnO_2 shell and hollow SiC core can induce conductive loss. (3) the conductive path between adjacent hollow spheres. In addition, SiC inside the MnO_2 cover has a low bandgap, which can increase electron transport and further

boost the conductance loss of the composite. Finally, stacking faults (SF), defects and vacancies in SiC and MnO_2 change the dielectric constant, generate more dipole polarisation, and lead to dipole relaxation loss, making it easier to attenuate the EMW energy. Based on the discussion above, the medium-size H-SiC@MnO_2-10 with the concentration of TEOS at 18 ml has the optimum EMW absorbing performance.

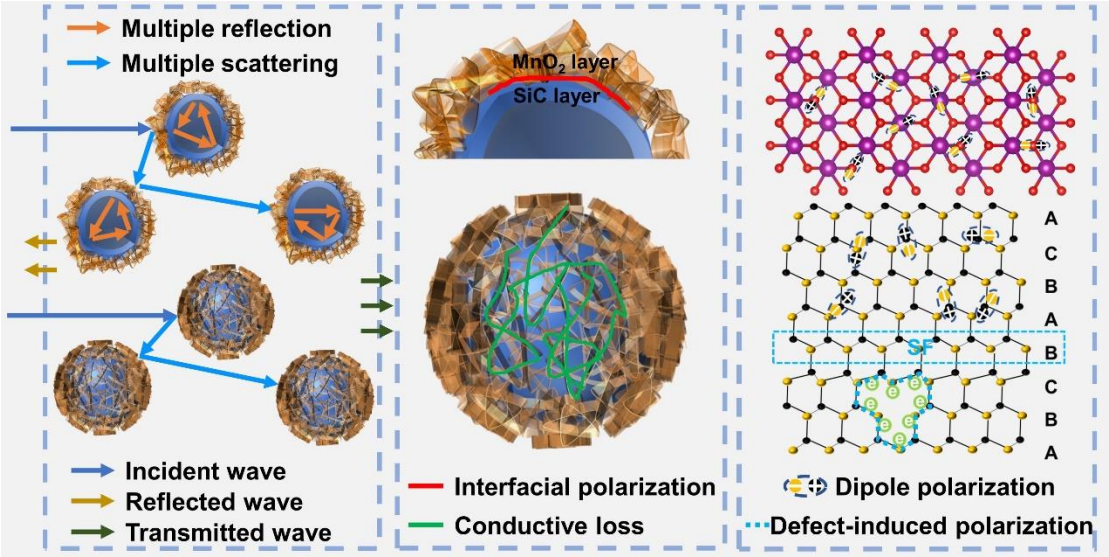

Figure 9 Schematic diagrams showing the EMW absorbing mechanisms.

4 Conclusions

In summary, a string of H-SiC@MnO_2 composites with size-tunable hollow spherical SiC core and thickness-tunable MnO_2 shell were successfully synthesised through carbon thermal reduction and hydrothermal reactions. The results show that the complex permittivity of the composites can be customised by adjusting the shell thickness and the core size. As expected, the hollow core-shell morphology of H-SiC@MnO_2 composites can improve the impedance matching condition and bring in multiple reflections of EMW. Moreover, the fully coated core-shell structure accelerates abundant heterogeneous interfaces, generating intense interfacial polarisation relaxation loss. Furthermore, the monodisperse and nanoscale characters of the composite enhance multiple scattering and reduce the ratio of reflection waves. When the concentration of $KMnO_4$ is 10 mM, and the volume of TEOS is 18 ml, the

prepared H-SiC@MnO_2 composite with 90 nm shell and 360 nm core has the highest EMW absorbing ability, and the ΔW_{10} can reach 5.71 GHz at only 1.8 mm. This work confirms that the H-SiC@MnO_2 composite is a very novel and potential EMW absorbing material.

Acknowledgements

This work is supported by the National Key R&D Program of China (2021YFB3502500) and the National Natural Science Foundation of China (52172091 and 52172295), Open Fund of Key Laboratory of Materials Preparation and Protection for Harsh Environment (Nanjing University of Aeronautics and Astronautics), Ministry of Industry and Information Technology (56XCA22042).

Declaration of competing interest

The authors declare no conflict of interest.

References

[1] C. Zhou, S. Geng, X. Xu, T. Wang, L. Zhang, X. Tian, F. Yang, H. Yang, Y. Li, Lightweight hollow carbon nanospheres with tunable sizes towards enhancement in microwave absorption, Carbon 108 (2016) 234-241. https://doi.org/10.1016/j.carbon.2016.07.015.

[2] B. Wei, M.Q. Wang, Z.J. Yao, Z.P. Chen, P. Chen, X.W. Tao, Y.J. Liu, J.T. Zhou, Bimetallic nanoarrays embedded in three-dimensional carbon foam as lightweight and efficient microwave absorbers, Carbon 191 (2022) 486-501. https://doi.org/10.1016/j.carbon.2022.02.020.

[3] W. Yang, J. Sun, W. Xu, Z. He, Y. Dong, Y. Fu, Y. Zhu, Development of wrinkled reduced graphene oxide wrapped polymer-derived carbon microspheres as viable microwave absorbents via a charge-driven self-assembly strategy, J Colloid Interface Sci 630 (2023) 34-45. https://doi.org/10.1016/j.jcis.2022.09.144.

[4] Z. Xu, M. He, Y. Zhou, M. Zhang, S. Feng, Y. Wang, R. Xu, H. Peng, X. Chen, Rime-like carbon paper@Bi2S3 hybrid structure for efficient and broadband microwave absorption, Chemical Engineering Journal 428 (2022). https://doi.org/10.1016/j.cej.2021.131127.

[5] B. Yang, J. Fang, C. Xu, H. Cao, R. Zhang, B. Zhao, M. Huang, X. Wang, H. Lv, R. Che, One-Dimensional Magnetic FeCoNi Alloy Toward Low-Frequency Electromagnetic Wave Absorption, Nano-Micro Letters 14 (2022). https://doi.org/10.1007/s40820-022-00920-7.

[6] Z. Xu, M. He, Y. Zhou, S. Nie, Y. Wang, Y. Huo, Y. Kang, R. Wang, R. Xu, H. Peng, X. Chen, Spider web-like carbonised bacterial cellulose/MoSe2 nanocomposite with enhanced microwave attenuation performance and tunable absorption bands, Nano Research 14 (2020) 738-746. https://doi.org/10.1007/s12274-020-3107-z.

[7] R. Wang, M. He, Y. Zhou, S. Nie, Y. Wang, W. Liu, Q. He, W. Wu, X. Bu, X. Yang, Metal−organic frameworks self-templated cubic hollow Co/N/C@MnO2 composites for electromagnetic wave absorption, Carbon 156 (2020) 378-388. https://doi.org/10.1016/j.carbon.2019.09.063.

[8] X. Su, Y. Liu, Z. Liao, Y. Bi, M. Ma, Y. Chen, Y. Ma, F. Wan, K.L. Chung, Recent progress of polyaniline-based composites in the field of microwave absorption, Synthetic Metals 291 (2022). https://doi.org/10.1016/j.synthmet.2022.117190.

[9] W. Yang, J. Sun, D. Liu, W. Fu, Y. Dong, Y. Fu, Y. Zhu, Rational design of hierarchical structure of carbon@polyaniline composite with enhanced microwave absorption properties, Carbon 194 (2022) 114-126. https://doi.org/10.1016/j.carbon.2022.03.061.

[10] W. Fu, W. Yang, C. Qian, Y. Fu, Y. Zhu, One-Pot Synthesis of Ag/AgCl Heterojunction Nanoparticles on Polyaniline Nanocone Arrays on Graphene Oxide for Microwave Absorption, ACS Applied Nano Materials 6 (2023) 3728-3737. https://doi.org/ 10.1021/acsanm.2c05440.

[11] M. He, Y. Zhou, T. Huang, S. Nie, Y. Wang, Z. Xu, Y. Huo, R. Xu, X. Chen, H. Peng, Flower-like CoS hierarchitectures@polyaniline organic-inorganic heterostructured composites: Preparation and enhanced microwave absorption performance, Composites Science and Technology 200 (2020). https://doi.org/10.1016/j.compscitech.2020.108403.

[12] X. Gu, W. Zhu, C. Jia, R. Zhao, W. Schmidt, Y. Wang, Synthesis and microwave absorbing properties of highly ordered mesoporous crystalline NiFe2O4, Chemical Communications 47 (2011) 5337-5339. https://doi.org/10.1039/c0cc05800a.

[13] X. Huang, J. Zhang, Z. Liu, T. Sang, B. Song, H. Zhu, C. Wong, Facile

preparation and microwave absorption properties of porous hollow BaFe12O19/CoFe2O4 composite microrods, Journal of Alloys and Compounds 648 (2015) 1072-1075. https://doi.org/10.1016/j.jallcom.2015.07.073.
[14] P. Melinon, B. Masenelli, F. Tournus, A. Perez, Playing with carbon and silicon at the nanoscale, Nature Materials 6 (2007) 479-490. https://doi.org/10.1038/nmat1914.
[15] Y. Wang, P. Xiao, W. Zhou, H. Luo, Z. Li, W. Chen, Y. Li, Microstructures, dielectric response and microwave absorption properties of polycarbosilane derived SiC powders, Ceramics International 44 (2018) 3606-3613. https://doi.org/10.1016/j.ceramint.2017.11.101.
[16] C. Liu, D. Yu, D.W. Kirk, Y. Xu, Porous silicon carbide derived from apple fruit with high electromagnetic absorption performance, Journal of Materials Chemistry C 4 (2016) 5349-5356. https://doi.org/10.1039/c6tc01319h.
[17] S.-C. Chiu, H.-C. Yu, Y.-Y. Li, High Electromagnetic Wave Absorption Performance of Silicon Carbide Nanowires in the Gigahertz Range, Journal of Physical Chemistry C 114 (2010) 1947-1952. https://doi.org/10.1021/jp905127t.
[18] T. Xiao, J. Kuang, H. Pu, Q. Zheng, Y. Lu, W. Liu, W. Cao, Hollow SiC microtube with multiple attenuation mechanisms for broadband electromagnetic wave absorption, Journal of Alloys and Compounds 862 (2021) 158032. https://doi.org/10.1016/j.jallcom.2020.158032.
[19] J. Zhou, B. Wei, Z. Yao, H. Lin, R. Tan, W. Chen, X. Guo, Preparation of hollow SiC spheres with biological template and research on its wave absorption properties, Journal of Alloys and Compounds 819 (2020) 153021. https://doi.org/10.1016/j.jallcom.2019.153021.
[20] C. Wang, T.C. You, Y.F. Zhang, M. Song, Z.Z. Huang, W.D. Xia, Synthesis of N-doped SiC nano-powders with effective microwave absorption and enhanced photoluminescence, Journal of Alloys and Compounds 932 (2023). https://doi.org/10.1016/j.jallcom.2022.167699.
[21] D. Dai, X. Lan, Z. Wang, Hierarchical carbon fiber reinforced SiC/C aerogels with efficient electromagnetic wave absorption properties, Composites Part B-Engineering 248 (2023). https://doi.org/10.1016/j.compositesb.2022.110376.
[22] Y. Zhang, J. He, Z. Fu, H. Yang, Lightweight porous NiCo-SiC aerogel with synergistically dielectric and magnetic losses to enhance electromagnetic wave absorption performances, Journal of Alloys and Compounds 926 (2022). https://doi.org/10.1016/j.jallcom.2022.166758.
[23] Z. Zhong, B. Zhang, J. Ye, Y. Ren, F. Ye, Tailorable microwave absorption properties of macro-porous core@shell structured SiC@Ti3SiC2 via molten salt shielded synthesis (MS3) method in air, Journal of Alloys and Compounds 927 (2022). https://doi.org/10.1016/j.jallcom.2022.167046.
[24] L. Yan, C. Hong, B. Sun, G. Zhao, Y. Cheng, S. Dong, D. Zhang, X. Zhang, In Situ Growth of Core-Sheath Heterostructural SiC Nanowire Arrays on Carbon Fibers and Enhanced Electromagnetic Wave Absorption Performance, ACS Appl Mater Interfaces 9 (2017) 6320-6331. https://doi.org/10.1021/acsami.6b15795.
[25] W. Li, W. Li, Y. Ying, J. Yu, J. Zheng, L. Qiao, J. Li, S. Che, Multifunctional flower-like core-shell Fe/Fe4N@SiO2 composites for broadband and high-efficiency ultrathin electromagnetic wave absorber, Journal of Materials Science & Technology 132 (2023) 90-99. https://doi.org/10.1016/j.jmst.2022.05.045.
[26] H. Lv, G. Ji, X. Liang, H. Zhang, Y. Du, A novel rod-like MnO2@Fe loading on graphene giving excellent electromagnetic absorption properties, Journal of Materials Chemistry C 3 (2015) 5056-5064. https://doi.org/10.1039/c5tc00525f.

[27] R. Yang, Y. Fan, R. Ye, Y. Tang, X. Cao, Z. Yin, Z. Zeng, MnO2-Based Materials for Environmental Applications, Advanced Materials 33 (2021). https://doi.org/10.1002/adma.202004862.
[28] X. Zhang, Z. Liu, B. Deng, L. Cai, Y. Dong, X. Zhu, W. Lu, Honeycomb-like NiCo2O4@MnO2 nanosheets array/3D porous expanded graphite hybrids for high-performance microwave absorber with hydrophobic and flame-retardant functions, Chemical Engineering Journal 419 (2021). https://doi.org/10.1016/j.cej.2021.129547.
[29] W. She, H. Bi, Z. Wen, Q. Liu, X. Zhao, J. Zhang, R. Che, Tunable Microwave Absorption Frequency by Aspect Ratio of Hollow Polydopamine@alpha-MnO2 Microspindles Studied by Electron Holography, ACS Appl Mater Interfaces 8 (2016) 9782-9789. https://doi.org/10.1021/acsami.6b00978.
[30] L. Yang, H. Lv, M. Li, Y. Zhang, J. Liu, Z. Yang, Multiple polarisation effect of shell evolution on hierarchical hollow C@MnO2 composites and their wideband electromagnetic wave absorption properties, Chemical Engineering Journal 392 (2020). https://doi.org/10.1016/j.cej.2019.123666.
[31] H. Guan, G. Chen, S. Zhang, Y. Wang, Microwave absorption characteristics of manganese dioxide with different crystalline phase and nanostructures, Materials Chemistry and Physics 124 (2010) 639-645. https://doi.org/10.1016/j.matchemphys.2010.07.027.
[32] M. Qiao, X. Lei, Y. Ma, L. Tian, K. Su, Q. Zhang, Dependency of tunable microwave absorption performance on morphology-controlled hierarchical shells for core-shell Fe3O4@MnO2 composite microspheres, Chemical Engineering Journal 304 (2016) 552-562. https://doi.org/10.1016/j.cej.2016.06.094.
[33] X. Li, L. Wang, W. You, L. Xing, L. Yang, X. Yu, J. Zhang, Y. Li, R. Che, Enhanced polarisation from flexible hierarchical MnO(2) arrays on cotton cloth with excellent microwave absorption, Nanoscale 11 (2019) 13269-13281. https://doi.org/10.1039/c9nr02667c.
[34] Y. Zhang, Z. Yang, M. Li, L. Yang, J. Liu, Y. Ha, R. Wu, Heterostructured CoFe@C@MnO2 nanocubes for efficient microwave absorption, Chemical Engineering Journal 382 (2020). https://doi.org/10.1016/j.cej.2019.123039.
[35] J. Liu, J. Tao, L. Gao, X. He, B. Wei, Y. Gu, Z. Yao, J. Zhou, Morphology-size synergy strategy of SiC@C nanoparticles towards lightweight and efficient microwave absorption, Chemical Engineering Journal 433 (2022) 134484. https://doi.org/10.1016/j.cej.2021.134484.
[36] J.A. Vigil, T.N. Lambert, J. Duay, C.J. Delker, T.E. Beechem, B.S. Swartzentruber, Nanoscale Carbon Modified alpha-MnO(2) Nanowires: Highly Active and Stable Oxygen Reduction Electrocatalysts with Low Carbon Content, ACS Appl Mater Interfaces 10 (2018) 2040-2050. https://doi.org/10.1021/acsami.7b16576.
[37] D. Pan, G. Yang, H.M. Abo-Dief, J. Dong, F. Su, C. Liu, Y. Li, B.B. Xu, V. Murugadoss, N. Naik, S.M. El-Bahy, Z.M. El-Bahy, M. Huang, Z. Guo, Vertically Aligned Silicon Carbide Nanowires/ Boron Nitride Cellulose Aerogel Networks Enhanced Thermal Conductivity and Electromagnetic Absorbing of Epoxy Composites, Nano-Micro Letters 14 (2022). https://doi.org/10.1007/s40820-022-00863-z.
[38] G. He, Y. Duan, L. Song, X. Zhang, Doping strategy to boost electromagnetic property and gigahertz tunable electromagnetic attenuation of hetero-structured manganese dioxide, Dalton Trans 48 (2019) 2407-2421. https://doi.org/10.1039/c8dt04372h.
[39] Z.N. Xiang, Y.Q. Wang, X.M. Yin, Q.C. He, Microwave absorption performance

of porous heterogeneous SiC/ SiO2 microspheres, Chemical Engineering Journal 451 (2023). https://doi.org/10.1016/j.cej.2022.138742.
[40] K. Sing, D. Everett, R. HAUL, L. MOSCOU, R. PIEROTTI, J. ROUQUEROL, T. SIEMIENIEWSKA, Reporting physisorption data for gas/solid systems with special reference to the determination of surface area and porosity, Pure and Applied Chemistry 57 (1985) 2201-2218. https://doi.org/10.1351/pac198254112201.
[41] H. Peng, X. Zhou, H. Lai, N. Wang, S. Lee, Microstructure observations of silicon carbide nanorods, Journal of Materials Research 15 (2000) 2020-2026. https://doi.org/10.1557/JMR.2000.0290.
[42] L.L. Xu, J.Q. Tao, X.F. Zhang, Z.J. Yao, A. Zavabeti, J.T. Zhou, Co@N-doped double-shell hollow carbon via self-templating-polymerisation strategy for microwave absorption, Carbon 188 (2022) 34-44. https://doi.org/10.1016/j.carbon.2021.11.043.
[43] J.Q. Tao, R.Y. Tan, L.L. Xu, J.T. Zhou, Z.J. Yao, Y.M. Lei, P. Chen, Z. Li, J.Z. Ou, Ion-Exchange Strategy for Metal-Organic Frameworks-Derived Composites with Tunable Hollow Porous and Microwave Absorption, Small Methods 6 (2022). https://doi.org/10.1002/smtd.202200429.
[44] X. Liu, X. Wang, H. Cui, Design and Property Analysis of Radar Absorbing Materials, National Defense Industry Press, Beijing, 2018.
[45] Z.B. Jiao, W.J. Huyan, J.R. Yao, Z.J. Yao, J.T. Zhou, P.J. Liu, Heterogeneous ZnO@CF structures and their excellent microwave absorbing properties with thin thickness and low filling, Journal of Materials Science & Technology 113 (2022) 166-174. https://doi.org/10.1016/j.jmst.2021.09.024.
[46] X.X. He, J.T. Zhou, J.Q. Tao, Y.J. Liu, B. Wei, Z.J. Yao, X.W. Tao, Preparation of porous CoNi/N-doped carbon microspheres based on magnetoelectric coupling strategy: A new choice against electromagnetic pollution, Journal of Colloid and Interface Science 626 (2022) 123-135. https://doi.org/10.1016/j.jcis.2022.06.153.
[47] J.T. Zhou, B. Wei, M.Q. Wang, Z.J. Yao, P. Chen, C.Y. Zhou, Z.J. Li, Three dimensional flower like ZnFe2O4 ferrite loaded graphene: Enhancing microwave absorption performance by constructing microcircuits, Journal of Alloys and Compounds 889 (2021). https://doi.org/10.1016/j.jallcom.2021.161734.
[48] J.Q. Tao, J.T. Zhou, Z.J. Yao, Z.B. Jiao, B. Wei, R.Y. Tan, Z. Li, Multi-shell hollow porous carbon nanoparticles with excellent microwave absorption properties, Carbon 172 (2021) 542-555. https://doi.org/10.1016/j.carbon.2020.10.062.
[49] M. He, H. Chen, H. Peng, Y. Zhou, Z. Song, Y. Wang, S. Feng, X. Bu, Ultralight Ti3C2Tx-derivative chrysanthemum-like Na2Ti3O7/Ti3C2Tx MXene quantum dots 3D/0D heterostructure with advanced microwave absorption performance, Chemical Engineering Journal 456 (2023).https://doi.org/ 10.1016/j.cej.2022.140985.
[50] H. Peng, M. He, Y. Zhou, Z. Song, Y. Wang, S. Feng, X. Chen, X. Zhang, H. Chen, Low-temperature carbonised biomimetic cellulose nanofiber/MXene composite membrane with excellent microwave absorption performance and tunable absorption bands, Chemical Engineering Journal 433 (2022). https://doi.org/10.1016/j.cej.2021.133269.
[51] J.B. Kim, S.K. Lee, C.G. Kim, Comparison study on the effect of carbon nano materials for single-layer microwave absorbers in X-band, Composites Science and Technology 68 (2008) 2909-2916. https://doi.org/10.1016/j.compscitech.2007.10.035.
[52] J.Q. Tao, L.L. Xu, L. Wan, J.S. Hou, P.S. Yi, P. Chen, J.T. Zhou, Z.J. Yao, Cubic-like Co/NC composites derived from ZIF-67 with a dual control strategy of size and graphitisation degree for microwave absorption, Nanoscale 13 (2021) 12896-12909. https://doi.org/10.1039/d1nr03450b.